

# Chemical Science

Accepted Manuscript

This article can be cited before page numbers have been issued, to do this please use: J. M. An, S. Kang, E. Huh, Y. Kim, D. Lee, H. Jo, J. F. F. Joung, V. J. Kim, J. Y. Lee, Y. S. Dho, Y. Jung, J. K. Hur, C. Park, J. Jung, Y. Huh, J. Ku, S. Kim, T. Chowdhury, S. Park, J. S. Kang, M. S. Oh, C. Park and D. Kim, *Chem. Sci.*, 2020, DOI: 10.1039/D0SC01085E.



This is an Accepted Manuscript, which has been through the Royal Society of Chemistry peer review process and has been accepted for publication.

Accepted Manuscripts are published online shortly after acceptance, before technical editing, formatting and proof reading. Using this free service, authors can make their results available to the community, in citable form, before we publish the edited article. We will replace this Accepted Manuscript with the edited and formatted Advance Article as soon as it is available.

You can find more information about Accepted Manuscripts in the [Information for Authors](#).

Please note that technical editing may introduce minor changes to the text and/or graphics, which may alter content. The journal's standard [Terms & Conditions](#) and the [Ethical guidelines](#) still apply. In no event shall the Royal Society of Chemistry be held responsible for any errors or omissions in this Accepted Manuscript or any consequences arising from the use of any information it contains.



## ARTICLE

## Penta-fluorophenol: A Smiles rearrangement-inspired cysteine-selective fluorescent probe for imaging of human glioblastoma

Jong Min An,<sup>a,†</sup> Sangrim Kang,<sup>b,c,†</sup> Eugene Huh,<sup>d,e,†</sup> Yejin Kim,<sup>f,g,†</sup> Dahae Lee,<sup>f</sup> Hyejung Jo,<sup>f</sup> Joonyoung F. Joung,<sup>h</sup> Veronica Jihyun Kim,<sup>i</sup> Ji Yeoun Lee,<sup>i,j</sup> Yun Sik Dho,<sup>k</sup> Yuna Jung,<sup>a</sup> Junho K. Hur,<sup>a,c</sup> Chan Park,<sup>a,b</sup> Junyang Jung,<sup>a,b</sup> Youngbuhm Huh,<sup>a,b</sup> Ja-Lok Ku,<sup>l</sup> Sojin Kim,<sup>k</sup> Tamrin Chowdhury,<sup>k</sup> Sungnam Park,<sup>h,\*</sup> Jae Seung Kang,<sup>f,g,\*</sup> Myung Sook Oh,<sup>d,m,\*</sup> Chul-Ke Park,<sup>k,\*</sup> and Dokyoung Kim,<sup>a,b,n,o,\*</sup>

Received 00th February 20xx,

Accepted 00th March 20xx

DOI: 10.1039/x0xx00000x

www.rsc.org/

One of the most critical factors for the survival of glioblastoma (GBM) patients is the precision diagnosis and the tracking of the treatment progress. At the moment, there are various sophisticated and specific diagnostic procedures being used, but there are relatively few simple diagnosis methods. This work introduces a sensing probe based on a turn-on type fluorescence response that can measure cysteine (Cys) level in the human-derived cells, as well as within on-site human clinical biopsy samples, which recognize Cys as a new biomarker of GBM. The Cys-initiated chemical reactions of the probe cause a significant fluorescence response with high selectivity, high sensitivity, a fast response time, and a two-photon excitable excitation pathway, which allows the imaging of GBM in both mouse models and human tissue samples. The probe can distinguish the GBM cells, as well as disease sites in clinical samples from individual patients. Besides, the probe has no short or long-term toxicity and immune response. The present findings hold promise for application of probe to a relatively simple and straightforward following of GBM at clinical sites.

## 1. Introduction

Glioblastoma (GBM) is the most aggressive form of cancer that originates within the central nervous system (CNS).<sup>1–3</sup> GBM represents 15% of all primary brain tumor,<sup>4</sup> but the cause is unclear, and there is no clear way to prevent it. Generally, the clinical management of GBM, including diagnosis, assessment progress, and therapy effectiveness evaluation have been mostly reliant on a neurological assessment and the clinical imaging technics, such as MRI (magnetic resonance imaging), CT (computed tomography), PET (positron emission tomography) and biopsy tissue sampling.<sup>5–8</sup>

In the era of precision medicine, the development of new tools for pathological analysis of GBM tissue biopsy samples has become prominent for various reasons, such as (i) consensus issue of histological diagnosis among pathologists, (ii) the need to improve the diagnostic yield within the limited samples due to the challengeable surgical approach, (iii) the need to improve the predictive values for disease progression, and (iv) the difficulties in performing repeated biopsies. In this vein, useful information of oncogenes, related to the key cellular mechanisms for GBM cells to survive, grow, and proliferate, holds potentials as an analytical tool for GBM.<sup>9–11</sup> For example, the precise monitoring of GBM genomic heterogeneity and mutational status, related to oncologic cellular mechanisms may well give beneficial information when selecting the treatment modalities. Another critical point is about the

<sup>a</sup> Department of Biomedical Science, Graduate School, Kyung Hee University, Seoul 02447 (Korea)

<sup>b</sup> Department of Anatomy and Neurobiology, College of Medicine, Kyung Hee University, Seoul 02447 (Korea)

<sup>c</sup> Department of Pathology, College of Medicine, Kyung Hee University, Seoul 02447 (Korea)

<sup>d</sup> Department of Medical Science of Meridian, Graduate School, Kyung Hee University, Seoul 02447 (Korea)

<sup>e</sup> Department of Life and Nanopharmaceutical Sciences, Graduate School, Kyung Hee University, Seoul 02447 (Korea)

<sup>f</sup> Laboratory of Vitamin C and Antioxidant Immunology, Department of Anatomy and Cell Biology, Seoul National University, College of Medicine, Seoul 03080 (Korea)

<sup>g</sup> Institute of Allergy and Clinical Immunology, Seoul National University Medical Research Center, Seoul 03080 (Korea)

<sup>h</sup> Department of Chemistry, Korea University, Seoul 02841 (Korea)

<sup>i</sup> Neural Development and Anomaly Laboratory, Department of Anatomy and Cell Biology, Seoul National University, College of Medicine, Seoul 03080, (Korea)

<sup>j</sup> Division of Pediatric Neurosurgery, Seoul National University, Children's Hospital, Seoul 03080 (Korea)

<sup>k</sup> Department of Neurosurgery, Seoul National University Hospital, Seoul National University, College of Medicine, Seoul 03080 (Korea)

<sup>l</sup> Korean Cell Line Bank, Cancer Research Institute, Seoul National University, College of Medicine, Seoul 03080 (Korea)

<sup>m</sup> Department of Oriental Pharmaceutical Science and Kyung Hee East-West Pharmaceutical Research Institute, Kyung Hee University, Seoul 02447, (Korea)

<sup>n</sup> Center for Converging Humanities, Kyung Hee University, Seoul 02447 (Korea)

<sup>o</sup> Medical Research Center for Bioreaction to Reactive Oxygen Species and Biomedical Science Institute, School of Medicine, Graduate School, Kyung Hee University, Seoul 02447 (Korea)

† Electronic Supplementary Information (ESI) available. See DOI: 10.1039/x0xx00000x

\* These authors contributed equally to this work.

\* E-mail: dskim@khu.ac.kr (D.K.), nsckpark@snu.ac.kr (C.-K.P.), msokhok@khu.ac.kr (M.S.O), genius29@snu.ac.kr (J.S.K.), spark8@korea.ac.kr (S.P.)



proposed monitoring of oncogenic metabolism related to glucose, hypoxia, fatty acid, and amino acid in GBM.<sup>9, 12–14</sup> Among them, we have observed dramatic changes in the amino acid level of GBM,<sup>15</sup> which was recognized in the clinical radioisotope imaging; increased levels of glutamate (Glu), glutamine (Gln), and methionine (Met), as well as a decreased level of aspartate (Asp). Such unusual amino acid levels in GBM could, therefore, be exploited by reprogramming the cellular metabolism and its sub-grouping of GBM, which is dependent on the amino acid level and is important, as a biomarker, for the precision diagnosis, therapy, and follow-up treatment.

In this study, we introduce a sensing probe, based on a turn-on type fluorescence response that can estimate cysteine (Cys) level in the human-derived GBM cell lines, xenograft animal model, and human biopsy samples. The Fluorescence-based diagnostic tools have been widely used at clinical sites because it is simple-to-operate, highly sensitive, selective, time-saving, economical, user-friendly, and highly applicable for bio-sample.<sup>16–21</sup> We have validated a newly developed probe which can isolate the GBM cells or tissues from healthy individuals, and examined its potential as a new tool in clinical pathology.

To date, many cases have provided evidence supporting the long-standing hypothesis that neural stem cell niche residents in the lateral ventricular (LV)-subventricular zone (SVZ) of the brain is the origin for GBM in humans (Fig. 1a).<sup>22</sup> GBM is affected by a high degree of hypoxia due to uncontrolled proliferation and defective vascularization.<sup>23</sup> In the hypoxia status, healthy cells die via apoptosis due to an increased level of intercellular reactive oxygen species (ROS), while the GBM cells can survive, grow, and infiltrate the organ (Fig. 1b).<sup>24–26</sup> The reason is that the increased transcription of the SLC7A11 gene in GBM is induced by the elevated ROS (Fig. 1c).<sup>27</sup> The elevated ROS level of the SLC7A11 gene that induces an over-expression of System Xc, a Cys/Glu transporter, located on the cell membrane, and System Xc lead the uptake of cystine (CySS) into the cell cytosol.<sup>28, 29</sup> In the endoplasmic reticulum (ER), the increased CySS is broken into two Cys by the over-expressed cysteine cathepsin, a cysteine protease enzyme that breaks disulfide links.<sup>30</sup> The resulting Cys became a precursor in the subsequent glutathione (GSH) synthesis with methionine that also overexpressed in GBM, and the resulting GSH produced played a vital role in the ROS attenuation.<sup>31</sup> As a result, GBM sustains its various characteristics in the hypoxia condition. No reports related with the direct monitoring of the Cys level in clinical GBM samples were disclosed, so we aim to introduce this as a new diagnostic tool to be used for the selective sensing of up-regulated Cys level in the human-derived cells, particularly in ER sub-organellar, and biopsy samples and propose Cys as a new biomarker of GBM within clinical pathology (Fig. 1d).

## 2. Results and discussion

### Rational

We recently focused on the development of a donor-acceptor (D-A) dipolar type fluorescent platform to monitor biologically

essential species, such as enzyme activity, cell organelles, metal ions, and disease biomarkers.<sup>32–35</sup> We designed a new molecular sensing platform based on nitrobenzoxadiazole (NBD) fluorophore, using various aromatic substitutions at the electron-donating site (R); simple phenol (NPO-A), electron-deficient penta-fluorophenol (NPO-B), and electron-rich p-methoxyphenol (NPO-C). As a control probe we used chloro-substituted NBD (NBD-Cl) (Fig. 2a). Interestingly, the addition-substitution of biothiols, such as Cys, homocysteine (Hcy), GSH, and hydrogen sulfide (H<sub>2</sub>S) occurred at the R-site, and the subsequent Smiles rearrangement (SR),<sup>36</sup> with amine-containing biothiols, showed a significant fluorescence response with the formation of D-A type dipolar dye (Fig. 2b). Previously, a similar approach based on the SR reaction for the thiol sensing has been reported,<sup>37–40</sup> and in this study, we asserted that the different electron density at the electron-donating site could cause different reaction rates toward biothiols. In particular, we hypothesize that the electron-deficient aromatic ring with penta-fluoro substitution (NPO-B) can make a unique hydrophobic macro-environment for amino acid coordination for SR and water molecules coordination, compared to the simple benzene ring in aqueous media. Besides, we hypothesize that the regulation of the level of Cys, that occurs in the ER for the penta-fluorophenol moiety towards ER targeting ability,<sup>41, 42</sup> makes it possible to trace the Cys level in the cells more precisely. With this novel rationale, we prepared the NPO series with the reaction of NBD-Cl and phenol derivatives in the presence of a base (Scheme S1). The purity of the synthesized compounds was verified by a proton/carbon nuclear magnetic resonance (<sup>1</sup>H/<sup>13</sup>C NMR) and high-resolution mass spectrometry (HRMS) (data in Supporting Information; SI).

### Sensing property of NPO probes

First, the selectivity assay of the NPO series was carried out in the presence of biothiols in aqueous media (deionized water; DI H<sub>2</sub>O) (Fig. 2c). Interestingly, NPO-B only showed very selective sensing ability toward Cys over the other thiols. The disturbance of Hcy was quite dramatic for NPO-A, NPO-C, and NBD-Cl, indicating that the SR reaction could be affected by the electron density of the leaving groups (R). The NPO-B showed a strong absorbance at 358 nm and 463 nm with negligible emission (Fig. 2d). The insufficient electron-donating ability and free-rotation of aromatic rings at R-site in aqueous media caused a low emission of NPO itself (Fig. S1). However, the treatment of Cys in the solution of NPO-B showed changes in absorbance (decrement at 340 nm, increment at 474 nm), with significant emission increments at 550 nm (20-fold) (Fig. 2d). After checking the non-aggregation factor of NPO-B (Fig. S2, a linear plot depends of concentration 1–100 μM), time-course fluorescence changes for the mixture of NPO series and biothiols were monitored in DI H<sub>2</sub>O, under excitation at the maximum absorption wavelength (474 nm) (Fig. 2e, Fig. S3–S6). A significant fluorescence enhancement was observed only in the mixture of NPO-B and Cys, and the signal was almost fully saturated within 10 min. In the concentration-dependent assay, NPO-B showed a high sensitivity under the given conditions, a



detection limit of 0.12 ppm, according to the signal-to-noise ratio above 3 (Fig. 2f). The optimal pH range for the sensing of Cys with NPO-B was found to be biological pHs (pH 5–8), including physiological pH (pH 7.4) (Fig. 2g, Fig. S7). In the selectivity assay, NPO-B only showed the fluorescence response towards Cys ("B" in Fig. 2h) among the biomolecules (biothiols, amino acids, protein) and metal ions. The selectivity of NPO-B was also verified within the Cys oxidation environment. Treatment of air bubbling and hydrogen peroxide ( $\text{H}_2\text{O}_2$ ) reduce the contents of Cys level, and we observed that the decreased emission intensity of NPO-B within these environments (Fig. S8). The cystine (CySS), which is a reduced form of Cys, showed no emission enhancement. We further investigated the selectivity of NPO-B with thiol substances (cysteamine, ethanethiol), which have a similar chemical structure with Cys (Fig. S8), and we found that a significant emission enhancement only for the Cys. Next, we performed the competitive experiments of NPO-B toward Cys and  $\text{H}_2\text{S}$  (Fig. S9). A similar emission enhancement of NPO-B was observed in the sets of Cys and the mixture of Cys with  $\text{H}_2\text{S}$ , not in the set of  $\text{H}_2\text{S}$  alone. These results indicate that the reaction of NPO-B is more favorable toward Cys than  $\text{H}_2\text{S}$ . The reaction product was analyzed using liquid chromatography mass spectrometry (LC-MS) to understand the sensing mechanism (Fig. S10). The reaction product of NPO-B and Cys showed 4 main peaks in LC-MS, which corresponded to the SR product (Cys amine-substitute), the disulfide-linked product between SR product and Cys, each disulfide-linked SR product, and pentafluorophenol side products. High photostability of the reaction mixture (NPO-B with Cys) was observed under a strong UV irradiation condition (Fig. S11a–S11c, >70% intensity over 60 min), which is one of the most substantial merits for the fluorescence-based bioimaging. Although absorption and emission intensity of reaction mixture (NPO-B with Cys) were decreased on the high temperature at 2 hours, we think that reaction mixture is stable enough to measure the bio-imaging results due to denaturation of cell and tissue more than at 40 °C (Fig. S11d–S11h).

### Quantum chemical calculation

To understand the selectivity of NPO-B toward Cys and the intramolecular substitution reaction of NPO-Cys and NPO-Hcy, we conducted quantum chemical calculations. All calculations were performed using the density functional theory (DFT) method with the APFD functional and 6-31g(d) basis set as implemented in the Gaussian 16 package.<sup>43</sup> The detailed calculation procedure is found in the SI. As shown in Fig. 2b, the NPO-B reacts with Cys (or Hcy) to form S-bound NPO-Cys (or NPO-Hcy), which further undergoes intramolecular substitution reactions to produce N-bound NPO-Cys (or NPO-Hcy), and the finally produced N-bound NPO-Cys emits strong fluorescence at 550 nm. First, we obtained the optimized structures of NPO-Cys and NPO-Hcy to investigate the stability of S-bound and N-bound isomers of NPO-Cys and NPO-Hcy. N-bound isomers are found to be more stable and favored than S-bound isomers (Fig. S12). Next, we further calculated the intrinsic reaction

coordinate (IRC) for the intramolecular substitution reaction (i.e., S-bound compounds are converted into N-bound compounds) of NPO-Cys and NPO-Hcy. In fact, the intramolecular substitution reactions of NPO-Cys and NPO-Hcy are accompanied by the proton transfer between NPO-Cys (or NPO-Hcy) and water molecules. Therefore, we calculated the intrinsic reaction coordinate (IRC) for the intramolecular substitution reaction of NPO-Cys with three water molecules and NPO-Hcy with four water molecules. Fig. S13 displays the energies and structures of S-bound compound, transition state (TS), and N-bound compound along the IRC and the final relaxed N-bound compound. As shown in Fig. S13, a five-membered ring is formed in the transition state (TS) of NPO-Cys with the simultaneous binding of both N and S atoms of Cys to NPO, whereas a six-membered ring is formed for the TS of NPO-Hcy. In the intramolecular substitution reaction, the TS energy is lower for NPO-Cys (five-membered ring configuration) than for NPO-Hcy (six-membered ring configuration), and additionally, the final N-bound compound is more stable for NPO-Cys than for NPO-Hcy. Overall, the intramolecular substitution reaction is more favored for NPO-Cys than for NPO-Hcy in terms of the TS and the energies of finally produced N-bound compounds. Note that in the IRC calculation, water solvation was not able to be fully calculated for a practical and technical reason, and thus, we used a limited number of water molecules for the IRC for the intramolecular substitution reaction of NPO-Cys and NPO-Hcy. Therefore, the energies of the S-bound compound, TS, and N-bound compound in the IRC might not be directly comparable with the experimental values, but the IRC calculation provides an essential insight into the difference in the intramolecular substitution reaction of NPO-Cys and NPO-Hcy.

### Applications in GBM cell lines

Considering the excellent specificity of NPO-B to trace Cys *in vitro*, we applied it to the bioimaging in various cell lines using confocal laser scanning microscopy (CLSM). After treatment of NPO-B, strong fluorescence signals were observed in the GBM cell lines, human primary GBM cell line (U87MG), and GBM patient-derived primary cultured cell line (SNU4098). The human ovarian cancer cell line (COV-318) showed a non-significant fluorescence intensity compared with the human embryonic kidney cell line (HEK293), a normal control cell. This data represents that the Cys level is much higher in GBM than other cells (Fig. 3a, Fig. S14–S15). The ER targeting ability of NPO-B was verified by co-staining, with ER tracer Red, Pearson correlation coefficient (PCC) value > 0.8 in cancer cell lines (Fig. 3b–3c, Fig. S16). Additionally, we checked other organelles (lysosome, nucleus, mitochondria) using each tracker (Fig. S17). The results showed higher PCC value in ER than in other organelles, indicating that the NPO-B can track ER with high specificity in U87MG cells (Fig. 3c, Fig. S17b). To understand the Cys-related cellular mechanism, we pre-incubated the external stimuli, Cys, CySS (a precursor of Cys), N-ethyl-maleimide (NEM, biothiol-scavenging reagent),<sup>44</sup> and erastin (inhibitor of system  $\text{X}_\text{c}$ )<sup>45</sup> (Fig. 3d). As we expected, the cells preincubated with Cys and CySS showed a stronger intensity than the cells incubated





with the probe only (Fig. 3e–3f). On the contrary, cells pretreated with NEM showed little intensity due to the inactivity of Cys (Fig. 3e). After external treatment with NEM, exogenous Cys cells showed a gradual fluorescent enhancement in the cells. The erastin-pretreated cells showed a significantly decreased intensity in the cells due to the blocking of system  $X_c$  (Fig. 3f). We additionally observed the fluorescence spectra from the vial and the cells (Fig. S18) and confirmed the well-overlapped spectra each other (Fig. S18e). We also compared the emission spectra from U87MG (GBM) and HEK293 (normal cells) and found higher emission intensity from the U87MG cells as we expected (Fig. S18f–S18g). We do think these results can prove the reaction of NPO-B with Cys in the cells (Fig. 3, Fig. S18), and U87MG has a higher concentration of Cys than HEK293. In the cell viability assay, a slightly decreased cell viability of NPO-B in high concentration (50  $\mu$ M) was observed in the GBM cell lines; SNU4098 (83%), U87MG (80%), while the other cell lines showed negligible viability changes (Fig. S19). Also, a slight volume decrease of cytosol for the U87MG cells was observed in the crystal-violet (CV) staining analysis (50  $\mu$ M NPO-B) (Fig. S20). We additionally checked the cell viability with pentafluorophenol, a side product of the reaction between NPO-B and Cys, and the result was very similar. This result indicated that more pentafluorophenol was generated in the GBM cell lines, which supported a higher level of Cys in these cell lines (Fig. S19b). This data proves that the fluorescence signal is generated by the reaction between NPO-B and intercellular Cys, and it is, therefore, possible to determine the level of Cys in the GBM cells.

### Applications in GBM xenograft model

Given that NPO-B has promising biocompatibility and Cys sensing ability with bio-imaging, we demonstrated the GBM tissue imaging with NPO-B in the GBM xenograft mouse model. The intracranial mouse model was prepared by unilateral injection of U87MG cells and SNU4098 cells to the brain, using stereotaxic apparatus (tumor-implantation), and the GBM formation was verified by the tissue analysis of the sacrificed brain (Fig. S21). We expected that NPO-B could penetrate into the brain by passing through the blood-brain barrier, and give a fluorescence enhancement in the GBM site (Fig. 4a). After intravenous injection of NPO-B (5 mg/kg) through the tail vein, the organs were sacrificed (45 min circulation) and then analyzed, using the fluorescence tissue imaging system (FTIS) (Fig. 4b–4d, 395 nm excitation, 500–550 nm detection channel). A strong fluorescence signal was observed in the GBM cell-implanted site of the mouse brain (U87MG for Fig. 4b, SNU4098 for Fig. 4c). A bio-distribution analysis based on the tissue Images showed that there was no significant fluorescence intensity in the organs, except the U87MG-implanted GBM site of the brain (intensity from kidney; remained blood, stomach; leftover food) (Fig. 4d). In the SNU4098-implanted xenograft mouse, a similar result was observed, but the liver also gave off a signal. The healthy mouse control set didn't show any signal in the brain under the given experimental conditions (Fig. S22). We also imaged the tissue samples with two-photon

microscopy (TPM). TPM based on nonlinear interaction between light and matter has emerged as an important tool for *in vivo* and *in vitro* imaging of tissues due to its various merits including: (i) excitation at near-infrared (NIR) wavelengths in biological window, which allows for deeper penetration, (ii) focal point excitation for high resolution with 3D image construction, (iii) minimal absorption through highly scattered tissue media, and (iv) suppressed photo-damage and bleaching to the tissues.<sup>46, 47</sup> In order to monitor the Cys level in each organ using TPM, we sacrificed the mouse organs and then treated NPO-B (100  $\mu$ M) for 60 min incubation at 37°C in phosphate-buffered saline (PBS) buffer (pH 7.4). As shown in Fig. 4e, strong fluorescence signals were observed in the GBM brain tissues compared to the healthy control set when excited at 900 nm (50 mW laser power at the focal point, detection channel: 458–527 nm). In z-stacked TPM images of each brain sample (20–100  $\mu$ m from the surface, 10  $\mu$ m regular intervals) with NPO-B, the signal was the strongest in the zone between 30  $\mu$ m and 70  $\mu$ m from the surface, representing the high tissue permeability of NPO-B and its sufficient deep tissue imaging ability under the TPM (Fig. 4f). The TPM intensity analysis result, at the different site of brain (healthy, GBM core, GBM periphery), showed that the signal from the GBM model was higher than the healthy control one, and the signal from core site was higher than the periphery site, indicating the higher Cys level in the GBM core site (Fig. 4g). In the TPM images of the other organs with NPO-B, strong fluorescence signals were mainly observed in the kidney, lung, spleen, and the heart for both GBM mouse models, U87MG-implanted and SNU4098-implanted (Fig. 4h, Fig. S23–S24). To evaluate the differences between the Cys levels in the blood of healthy and GBM mouse models, we treated NPO-B to the extracted plasma, and then checked the fluorescence intensities (Fig. 4i). We observed a slightly lower intensity in the plasma of the GBM model, but it was not significant. In the fluorescence signal analysis of the mouse plasma, after intravenous treatment of NPO-B (5 mg/kg, 45 min circulation), fluorescence signals were not observed. This data represented that NPO-B seemed to be accumulated in the GBM site and some organs, reacting with Cys, but not a significant reaction with Cys in the blood (Fig. 4j).

### Applications in GBM human clinical samples

For the practical application of NPO-B, we finally applied NPO-B to the GBM human clinical samples. The excisional biopsy brain tissues were collected during the brain surgery and GBM-patient surgery (number of samples: normal=15, GBM=15, normal-GBM interface=5. See the patient information in Table S2), and then analyzed by FTIS and TPM imaging after the treatment of NPO-B (Fig. 5a). First, each site was verified by pathological analysis with H&E staining, and it clearly showed an abnormality for the GBM site (Fig. 5b). Generally, this kind of pathological analysis is essential for disease confirmation, as well as grade decisions, but it is time-consuming (it takes several days for staining) with a complicated procedure, and highly dependent on the pathologist's opinion.<sup>48</sup> In this aspect, NPO-B shows strong merits to overcome the drawbacks of the present



methods and is offered as a complementary new diagnostic tool. We treated NPO-B to the tissue samples (100  $\mu$ M) for 30 min incubation at 37  $^{\circ}$ C in the PBS buffer (pH 7.4) and monitored fluorescence intensities using FTIS (Fig. 5c) and TPM (Fig. 5d, Fig. S25–S26). Similar to the GBM xenograft mouse results, a significantly much higher fluorescence signal was observed in the GBM tissues than in normal tissues within TPM images (Fig. 5e). The tissue sample of the normal-GBM interface (periphery) also showed higher intensity than the normal tissues (Fig. S26). We then analyzed the TPM intensities in different gender (male=14, female=16, Fig. 5f) and ages (Fig. 5g). As we expected, the GBM group showed higher intensity than the normal group, but the gender-dependent intensity differences were not observed in normal and the GBM group, respectively. In the age-dependent plotting, the older GBM group gave a higher intensity, and the eighty-plus were approximately twice as high as the normal. The tissue sample of normal-GBM interface (periphery) also showed higher intensity than the normal tissue (Fig. S26). We confirmed the TPM emission spectra between solutions and biopsy via lambda screening of whole spectrum (Fig. S27) and found the well-overlapped fluorescence spectra from the confocal dish (Fig. S27a, NPO-B with Cys) and biopsy samples (Fig. S27b, NPO-B treated). This result indicated that the fluorescence signal from biopsy samples was generated from the reaction of NPO-B and Cys. These practical application results represented that the level of Cys is significantly higher in the GBM patient, and it can be considered as a new biomarker for the diagnosis and prognosis of GBM.

### In vivo immune-toxicity analysis

With the promising GBM imaging results, the toxic effects of NPO-B in the liver, renal toxicity, and immuno-toxicity were investigated for the practical application, such as the spraying of NPO-B towards the surgical site of a GBM patient's brain. The toxicity of NPO-B was analyzed in the healthy mouse (C57BL/6J, i.v. injection), and the results were compared with positive control, lipopolysaccharide (LPS) treated set.<sup>49</sup> As shown in Fig. S28a and S28b, neither morphological nor histological change in the liver and kidney was observed in the NPO-B treated set (24 h, 48 h circulation), while the LPS treated group showed significant changes. Besides, no apparent changes in the spleen and lymph nodes were observed. Next, the hematological and immunological parameters, which were related to organ damages and immunotoxicity, were examined. After the administration of NPO-B (5 mg/kg) and LPS (10  $\mu$ g/animal), blood was collected from the intra-orbital plexus, and the changes of aspartate aminotransferase (AST) and alanine aminotransferase (ALT),<sup>50</sup> which are general markers for hepatic damages, were examined. The NPO-treated group showed no significant values, but the LPS-treated group showed a remarkably increased value (Fig. S28c). The NPO-B treated set also gave no increment of IL-6, IL-1 $\beta$ , and TNF- $\alpha$ , which are major inflammatory cytokines (Fig. S28d).<sup>51</sup> The enlargement of the spleen and lymph node means an increase of proliferation of the immune cells, and so we compared the immune cell

numbers and stimulation index between both NPO-B and LPS treated groups. As a result, we found that there was no increase of the immune cell numbers and the stimulation index<sup>52</sup> in the NPO-B treated group (Fig. S28e). No CD69 factor change, which is increased by inguinal lymph node cell proliferation, as an early activation marker, was monitored in the NPO-B treated set (Fig. S28f). Together, no effect of NPO-B, related to the population of other types of immune cells, including NK cells, B cells, and macrophages, was observed (Fig. S28g). NPO-B showed no short-term hepatotoxicity, based on changes in AST and ALT, which suggested that NPO-B is a highly safe contrast agent without any short- or long-term toxicity in the liver and kidney. In the toxicity assay, NPO-B didn't show any toxicity in the liver or kidney, as well as in any immune organs, which proves that NPO-B can be safely applied in a clinical approach, not only for healthy people but also for the patient.

### 3. Conclusions

These simple methods to monitor the presence or recurrence of brain cancer, particularly GBM, are invaluable tools to improve the outcomes in a patient's treatment. In this study, we have reported a small molecular probe that addresses this challenge targeting Cys, which is a new biomarker of GBM. We created and characterized a turn-on type fluorescent probe, NPO-B, that allows the tracing of Cys with high selectivity, sensitivity, and biocompatibility. We applied the probe for the first time to monitor the Cys level in human-derived GBM cell lines, a GBM xenograft mouse model, and human clinical biopsy GBM samples. We then systematically analyzed its photophysical properties and provided the sensing mechanism at in vitro as well as the cell lines. The NPO-B treated GBM cell lines showed a bright fluorescence under the CLSM, and it also worked in the GBM-site imaging of the xenograft mouse model, using FTIS and TPM. Furthermore, we found the probe could distinguish the GBM site of patients from the healthy control through fluorescence analysis of the TPM tissue samples. In presenting our findings, we firmly believe that they show great promise for the application of NPO-B to create a relatively simple and straightforward screening of GBM from the excisional biopsy brain tissues, and this can be used to replace the current complex protocols. The lack of short-/long-term toxicity and immune response results also shows that NPO-B can be fully utilized throughout the various clinical applications. In addition to the diagnostic applications, the probe alone or the hybridization with nanoparticles of the probe has the potential to be applied to image-guided tumor resection, all of which could benefit from a selective fluorescence probe that senses Cys.

### 4. Methods

#### General information vivo immune-toxicity analysis

Supporting Information is available for the reagents, instruments, and analytical methods in this study.



## ARTICLE

## CHEMICAL SCIENCE

## Synthesis of NPO series

NPO series were prepared with the reaction of 4-chloro-7-dinitrobenzofurazan and phenol derivatives in the presence of base. See details in Supporting Information (Scheme S1) and synthetic protocols.

## Cell culture

Human primary glioblastoma cell line (U87 MG), immortalized human cervical cancer cell line (HeLa), human ovarian cancer cell line (COV-318), and human embryonic kidney cell line (HEK293) were obtained from Korean Cell Line Bank. Cells were cultured in Dulbecco's modified Eagle's media (Hyclone, US) supplemented with 10% fetal bovine serum (Hyclone) and 1% penicillin-streptomycin (Gibco). Glioblastoma cell line (SNU4098) was isolated from human GBM tissues (patient-derived clinical sample) and it was obtained from Korean Cell Line Bank. The SNU4098 cells were cultured in Opti-MEM, supplemented with 5% fetal bovine serum (Gibco™, US) and 1% antibiotic-antimycotic (Gibco™, US). Cell lines were kept in humidified air, containing 5% CO<sub>2</sub> at 37 °C.

## Animals

6-week-old female BALB/c nu/nu mice (Taconic, provided by Daehan Biolink Co., Ltd., Eumseong, Rep. of Korea) were housed at an ambient temperature of 23 ± 1 °C and relative humidity of 60 ± 10% under a 12 h light/dark cycle, and were allowed free access to water and food. All of the experiments performed with mice were carried out in accordance with the National Institute of Health Guide for the Care and Use of Laboratory Animals (NIH Publications No. 80-23) revised in 1996 and protocols approved by the Institutional Animal Care and Use Committee of Kyung Hee University (KHUASP(SE)-19-002).

## Intracranial xenograft (tumor implantation) animal model

U87MG and SNU4098 cell lines were used for the xenograft. Mice were anesthetized with tribromoethanol (312.5 mg/kg, i.p.) and mounted in a stereotaxic apparatus (myNeuroLab, St. Louis, MO, USA). Each mouse received a unilateral injection of 1.0 × 10<sup>6</sup> U87MG cells or SNU4098 cells per 5 µL in medium without FBS, according to the following coordinates: anteroposterior: -3.0 mm from bregma; mediolateral: 1.8 mm from bregma; and dorsoventral: -3.0 mm from the skull. The flow for the injection was regulated using an electronic pump at 1 µL/min for 5 min and followed by 2 min with a needle at the injection site to avoid reflux. Sham operations followed the same procedure for the infusion of the medium without FBS. After surgery, mice were allowed to recover from anesthesia in a temperature-controlled chamber and then placed in individual cages.

## Ex vivo tissue fluorescence imaging

VISQUE® InVivo Elite (Vieworks Co., Ltd., Rep. of Korea) was used as an ex vivo fluorescence tissue imaging system (FTIS). The imaging experiment was carried out in a dark room (wrapped in aluminum foil).

(A) *Animal samples*: After intravenously injection of NPO-B, mouse organs (brain, lung, heart, liver, spleen, colon and kidney) were isolated and washed with PBS buffer (3 times). Then, the ex vivo tissue imaging experiment for tissues was conducted. Brain: lens zoom: 6×, focus: 0.0 cm, iris: F3.6, mode: GFP, LED: Blue, type: single-frame, exposure time: 5 sec, binning: 1×1, intensity min=170.0, max=480.0). Other organs: lens zoom: 3×, focus: 1.0 cm, iris: F3.6, mode: GFP, LED: Blue, type: single-frame, exposure time: 5 sec, binning: 1×1, intensity min=170.0, max=480.0.

(B) *Human samples*: Human tissue samples were washed with PBS buffer (3 times) and treated with NPO-B (100 µM) for 30 min. After incubation, the tissue samples were washed with PBS buffer (3 times) to remove remaining NPO-B. Next, the tissue samples were washed again with PBS buffer (3 times) and treated with 4% PFA to fix for 30 min. The imaging experiment was conducted, washing the tissues with PBS buffer (3 times) again before imaging. Condition: lens zoom: 2.5×, focus: 1.5 cm, iris: F2.5, mode: GFP, LED: Blue, type: single-frame, exposure time: 1 sec, binning: 1×1, intensity min=1031.0, max=3218.6.

## Two-photon microscopy (TPM) tissue imaging

The imaging experiment was carried out in a dark room; tissues samples were wrapped in aluminum. The scanning two-photon microscopy (TPM, Leica, Nussloch, Germany) equipped with a Titanium Sapphire laser (Chameleon vision, Coherent, USA) and 25× water immersion objective lens was used for ex vivo imaging of these tissue samples. Two-photon excitation at 900 nm with laser power of approximately 50 mW at the focal plane provided the best image quality. Fluorescence intensity of TPM images were analyzed using Leica software (Germany) and Image-J (NIH, USA).

(A) *Animal samples*: Mice were anesthetized and perfused transcardially with PBS buffer (0.05 M). The mice were dissected to isolate organs: brain, lung, liver, kidney, spleen, colon, heart and stomach and to perform further ex vivo studies. Each organ was washed with PBS buffer (3 times). The mice tissues were placed in dry ice for 5 min. After this, frozen organs were cut into several pieces by surgical blade (NO.11, Reather safety razor Co., LTD, Japan). The sliced tissue samples showed an average thickness of about 100 µm, and were transferred into a 24 well plate (SPL Life Science, Rep. of Korea), and washed with PBS buffer (3 times). Next, NPO-B (100 µM) was treated and incubated for 1 h at 37 °C in a shaking incubator. After incubation, the tissue samples were washed with PBS buffer (3 times), and treated with 4% PFA for the tissue fixation. Two-photon microscopy (TPM) imaging experiments were conducted with additional washing of tissues with PBS buffer (3 times).

(B) *Human samples*: Patient-derived human clinical samples (GBM) assay with TPM used the same method described above.

## Human GBM samples

The human GBM tissue samples were snap-frozen in liquid nitrogen immediately during the surgery and were stored at -80 °C. This study was approved by the Institutional Review Boards (IRB) of Seoul National University Hospital (#H-1404-056-572).





## ARTICLE

## CHEMICAL SCIENCE

## Immuno-toxicity analysis

C57BL/6J mice were kept in a specific pathogen-free condition in the animal facility at Seoul National University College of Medicine (Rep. of Korea). Six-to eight-week old male mice weighing 20–25 g were used for the experiments. The animal protocol for the experiments was reviewed and approved by Ethics Committee of Seoul National University. See more details in Supporting Information.

## Conflicts of interest

The authors declare the following competing financial interest(s): The authors are listed as inventors on a pending patent application related to technology described in this work.

## Acknowledgements

This research was supported by the Bio & Medical Technology Development Program of the National Research Foundation (NRF) of Korea funded by the Ministry of Science & ICT (2018-M3A9H3021707) and by the Medical Research Center Program (2017-R1A5A2014768, 2019-M3A9H1103783). This research was also supported by the Basic Science Research Program of the NRF of Korea funded by the Ministry of Education (2018-R1A6A1A03025124, 2018-R1D1A1B07043383). This research was also supported by the NRF of Korea (2017-R1A2B2010948 for J.S.K., 2017-R1E1A1A01074529 for J.K.H., and 2019-R1A6A1A11044070 for S.P.).

## Notes and references

- M. Weller, W. Wick, K. Aldape, M. Brada, M. Berger, S. M. Pfister, R. Nishikawa, M. Rosenthal, P. Y. Wen, R. Stupp and G. Reifenberger, *Nat. Rev. Dis. Primers*, 2015, **1**, 15017.
- K. Aldape, K. M. Brindle, L. Chesler, R. Chopra, A. Gajjar, M. R. Gilbert, N. Gottardo, D. H. Gutmann, D. Hargrave, E. C. Holland, D. T. W. Jones, J. A. Joyce, P. Kearns, M. W. Kieran, I. K. Mellinghoff, M. Merchant, S. M. Pfister, S. M. Pollard, V. Ramaswamy, J. N. Rich, G. W. Robinson, D. H. Rowitch, J. H. Sampson, M. D. Taylor, P. Workman and R. J. Gilbertson, *Nat. Rev. Clin. Oncol.*, 2019, **16**, 509–520.
- D. N. Louis, A. Perry, G. Reifenberger, A. von Deimling, D. Figarella-Branger, W. K. Cavenee, H. Ohgaki, O. D. Wiestler, P. Kleihues and D. W. Ellison, *Acta Neuropathol.*, 2016, **131**, 803–820.
- Q. T. Ostrom, H. Gittleman, G. Truitt, A. Boscia, C. Kruchko and J. S. Barnholtz-Sloan, *Neuro Oncol*, 2018, **20**, iv1–iv86.
- G. Shukla, G. S. Alexander, S. Bakas, R. Nikam, K. Talekar, J. D. Palmer and W. Shi, *Chin Clin Oncol*, 2017, **6**, 40.
- K. Yamashita, A. Hiwatashi, O. Togao, K. Kikuchi, R. Hatae, K. Yoshimoto, M. Mizoguchi, S. O. Suzuki, T. Yoshiura and H. Honda, *AJNR Am.*, 2016, **37**, 58–65.
- H.-W. Kao, S.-W. Chiang, H.-W. Chung, F. Y. Tsai and C.-Y. Chen, *BioMed Res. Int.*, 2013, **2013**, 14.
- K. Weigel, *Neurosurgery*, 2019, **84**, E273–E273.
- M. M. Kim, A. Parolia, M. P. Dunphy and S. Venneti, *Nat Rev Clin Oncol*, 2016, **13**, 725–739.
- D. S. Nørøxe, H. S. Poulsen and U. Lassen, *ESMO Open*, 2016, **1**, e000144. DOI: 10.1039/D0SC01085E
- A. Shergalis, A. Bankhead, 3rd, U. Luesakul, N. Muangsins and N. Neamati, *Pharmacol Rev*, 2018, **70**, 412–445.
- Y. Zhou, L. Yang, X. Zhang, R. Chen, X. Chen, W. Tang and M. Zhang, *Biomed Res Int*, 2019, **2019**, 6581576.
- W. X. Mai, L. Gosa, V. W. Daniels, L. Ta, J. E. Tsang, B. Higgins, W. B. Gilmore, N. A. Bayley, M. D. Harati, J. T. Lee, W. H. Yong, H. I. Kornblum, S. J. Bensinger, P. S. Mischel, P. N. Rao, P. M. Clark, T. F. Cloughesy, A. Letai and D. A. Nathanson, *Nat Med*, 2017, **23**, 1342.
- Z. Dong and H. Cui, *Seminars in Cancer Biology*, 2019, **57**, 45–51.
- S. Liu, H. Ma, Z. Zhang, L. Lin, G. Yuan, X. Tang, D. Nie, S. Jiang, G. Yang and G. Tang, *Theranostics*, 2019, **9**, 1144–1153.
- H.-W. Liu, L. Chen, C. Xu, Z. Li, H. Zhang, X.-B. Zhang and W. Tan, *Chem. Soc. Rev.*, 2018, **47**, 7140–7180.
- Y. Tang, D. Lee, J. Wang, G. Li, J. Yu, W. Lin and J. Yoon, *Chem. Soc. Rev.*, 2015, **44**, 5003–5015.
- M. Gao, F. Yu, C. Lv, J. Choo and L. Chen, *Chem. Soc. Rev.*, 2017, **46**, 2237–2271.
- J. Zhang, X. Chai, X.-P. He, H.-J. Kim, J. Yoon and H. Tian, *Chem. Soc. Rev.*, 2019, **48**, 683–722.
- L.-Y. Niu, Y.-Z. Chen, H.-R. Zheng, L.-Z. Wu, C.-H. Tung and Q.-Z. Yang, *Chem. Soc. Rev.*, 2015, **44**, 6143–6160.
- J. Chan, S. C. Dodani and C. J. Chang, *Nat. Chem.*, 2012, **4**, 973.
- S. Facchino, M. Abdouh and G. Bernier, *Cancers (Basel)*, 2011, **3**, 1777–1797.
- S. Jawhari, M.-H. Ratinaud and M. Verdier, *Cell Death Dis.*, 2016, **7**, e2434.
- E. Singer, J. Judkins, N. Salomonis, L. Matlaf, P. Soteropoulos, S. McAllister and L. Soroceanu, *Cell Death Dis.*, 2015, **6**, e1601.
- A. R. Monteiro, R. Hill, G. J. Pilkington and P. A. Madureira, *Cells*, 2017, **6**, 45.
- W.-J. Huang, W.-W. Chen and X. Zhang, *Oncol Lett*, 2016, **12**, 2283–2288.
- P. M. D., R.-T. R. F., C. G. A., M. G. K. and A. K. S., *Stem Cells Dev.*, 2017, **26**, 1236–1246.
- M. D. Polewski, R. F. Reveron-Thornton, G. A. Cherryholmes, G. K. Marinov, K. Cassady and K. S. Aboody, *Mol. Cancer Res.*, 2016, **14**, 1229–1242.
- R. J. Bridges, N. R. Natale and S. A. Patel, *Br J Pharmacol*, 2012, **165**, 20–34.
- R. Löser and J. Pietzsch, *Front Chem*, 2015, **3**, 37–37.
- T. A. Ogunrinu and H. Sontheimer, *J. Biol. Chem.*, 2010, **285**, 37716–37724.
- D. Kim, H. Moon, S. H. Baik, S. Singha, Y. W. Jun, T. Wang, K. H. Kim, B. S. Park, J. Jung, I. Mook-Jung and K. H. Ahn, *J. Am. Chem. Soc.*, 2015, **137**, 6781–6789.
- D. Kim, S. H. Baik, S. Kang, S. W. Cho, J. Bae, M.-Y. Cha, M. J. Sailor, I. Mook-Jung and K. H. Ahn, *ACS Cent. Sci.*, 2016, **2**, 967–975.
- Y. Jung, Y. Kim, N. H. Kim, J. Lee, K.-H. Kim, J. Jung, Y. Huh, H.-J. Jang, J. Joo, S. Park and D. Kim, *Dyes Pigm.*, 2019, **162**, 104–111.
- H. Moon, Y. Jung, Y. Kim, B. W. Kim, J. G. Choi, N. H. Kim, M. S. Oh, S. Park, B. M. Kim and D. Kim, *Org. Lett.*, 2019, **21**, 3891–3894.





## ARTICLE

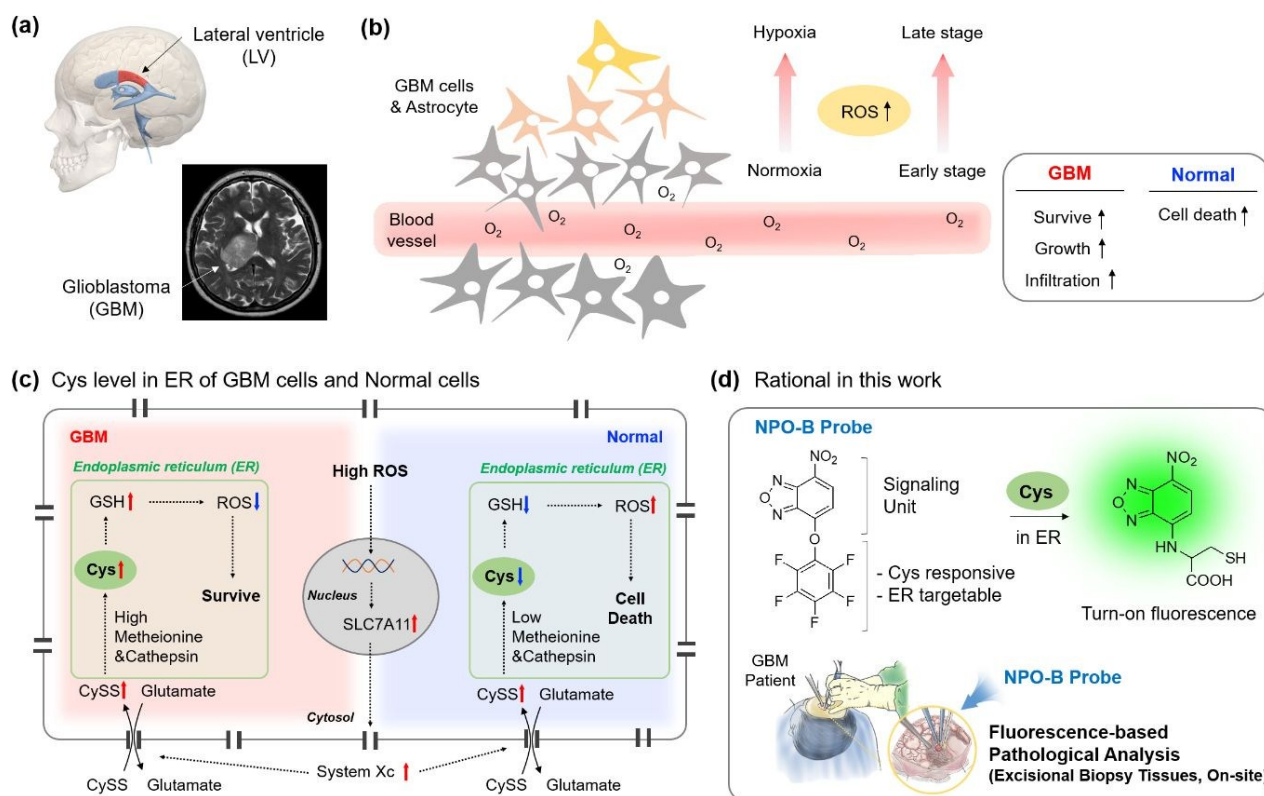
## CHEMICAL SCIENCE

36. C. M. Holden and M. F. Greaney, *Chem. Eur. J.*, 2017, **23**, 8992-9008.
37. M. D. Hammers and M. D. Pluth, *Anal. Chem.*, 2014, **86**, 7135-7140.
38. X. Dai, Z.-Y. Wang, Z.-F. Du, J. Cui, J.-Y. Miao and B.-X. Zhao, *Anal. Chim. Acta*, 2015, **900**, 103-110.
39. J. Wang, L. Niu, J. Huang, Z. Yan, X. Zhou and J. Wang, *Dyes Pigm.*, 2018, **158**, 151-156.
40. P. Wang, Y. Wang, N. Li, J. Huang, Q. Wang and Y. Gu, *Sens. Actuators B Chem.*, 2017, **245**, 297-304.
41. A. Goujon, A. Colom, K. Straková, V. Mercier, D. Mahedic, S. Manley, N. Sakai, A. Roux and S. Matile, *J. Am. Chem. Soc.*, 2019, **141**, 3380-3384.
42. N. Wagner, M. Stephan, D. Höglinger and A. Nadler, *Angew. Chem. Int. Ed.*, 2018, **57**, 13339-13343.
43. G. W. T. M. J. Frisch, H. B. Schlegel, G. E. Scuseria, M. A. Robb, J. R. Cheeseman, G. Scalmani, V. Barone, G. A. Petersson, H. Nakatsuji, X. Li, M. Caricato, A. V. Marenich, J. Bloino, B. G. Janesko, R. Gomperts, B. Mennucci, H. P. Hratchian, J. V. Ortiz, A. F. Izmaylov, J. L. Sonnenberg, D. Williams-Young, F. Ding, F. Lipparini, F. Egidi, J. Goings, B. Peng, A. Petrone, T. Henderson, D. Ranasinghe, V. G. Zakrzewski, J. Gao, N. Rega, G. Zheng, W. Liang, M. Hada, M. Ehara, K. Toyota, R. Fukuda, J. Hasegawa, M. Ishida, T. Nakajima, Y. Honda, O. Kitao, H. Nakai, T. Vreven, K. Throssell, J. A. Montgomery, Jr., J. E. Peralta, F. Ogliaro, M. J. Bearpark, J. J. Heyd, E. N. Brothers, K. N. Kudin, V. N. Staroverov, T. A. Keith, R. Kobayashi, J. Normand, K. Raghavachari, A. P. Rendell, J. C. Burant, S. S. Iyengar, J. Tomasi, M. Cossi, J. M. Millam, M. Klene, C. Adamo, R. Cammi, J. W. Ochterski, R. L. Martin, K. Morokuma, O. Farkas, J. B. Foresman, and D. J. Fox, Gaussian 16 (Revision B.01), Gaussian Inc., Wallingford, CT, 2016.
44. C. R. Yellaturu, M. Bhanoori, I. Neeli and G. N. Rao, *J. Biol. Chem.*, 2002, **277**, 40148-40155.
45. M. Sato, R. Kusumi, S. Hamashima, S. Kobayashi, S. Sasaki, Y. Komiyama, T. Izumikawa, M. Conrad, S. Bannai and H. Sato, *Sci. Rep.*, 2018, **8**, 968.
46. W. Denk, J. Strickler and W. Webb, *Science*, 1990, **248**, 73-76.
47. H. M. Kim and B. R. Cho, *Chem. Rev.*, 2015, **115**, 5014-5055.
48. A. Ruiz, O. Sertel, M. Ujaldon, U. Catalyurek, J. Saltz and M. Gurcan, 2007.
49. M. Ogata, S. Yoshida, M. Kamochi, A. Shigematsu and Y. Mizuguchi, *Infect. Immun.*, 1991, **59**, 679-683.
50. F. Sherer, G. V. Simaey, J. Kers, Q. Yuan, G. Doumont, M.-A. Laute, C. Peleman, D. Egrise, TonyLahoutte, V. Flamand and S. Goldman, *J. Liver*, 2015, **4**, 1000170.
51. S. Copeland, H. S. Warren, S. F. Lowry, S. E. Calvano and D. Remick, *Clin. Diagn. Lab Immunol.*, 2005, **12**, 60-67.
52. R. I. de Ávila, M. de Sousa Vieira, M. P. N. Gaeti, L. C. Moreira, L. de Brito Rodrigues, G. A. R. de Oliveira, A. C. Batista, D. C. Vinhal, R. Menegatti and M. C. Valadares, *Toxicology*, 2017, **376**, 83-93.

View Article Online  
DOI: 10.1039/D0SC01085E

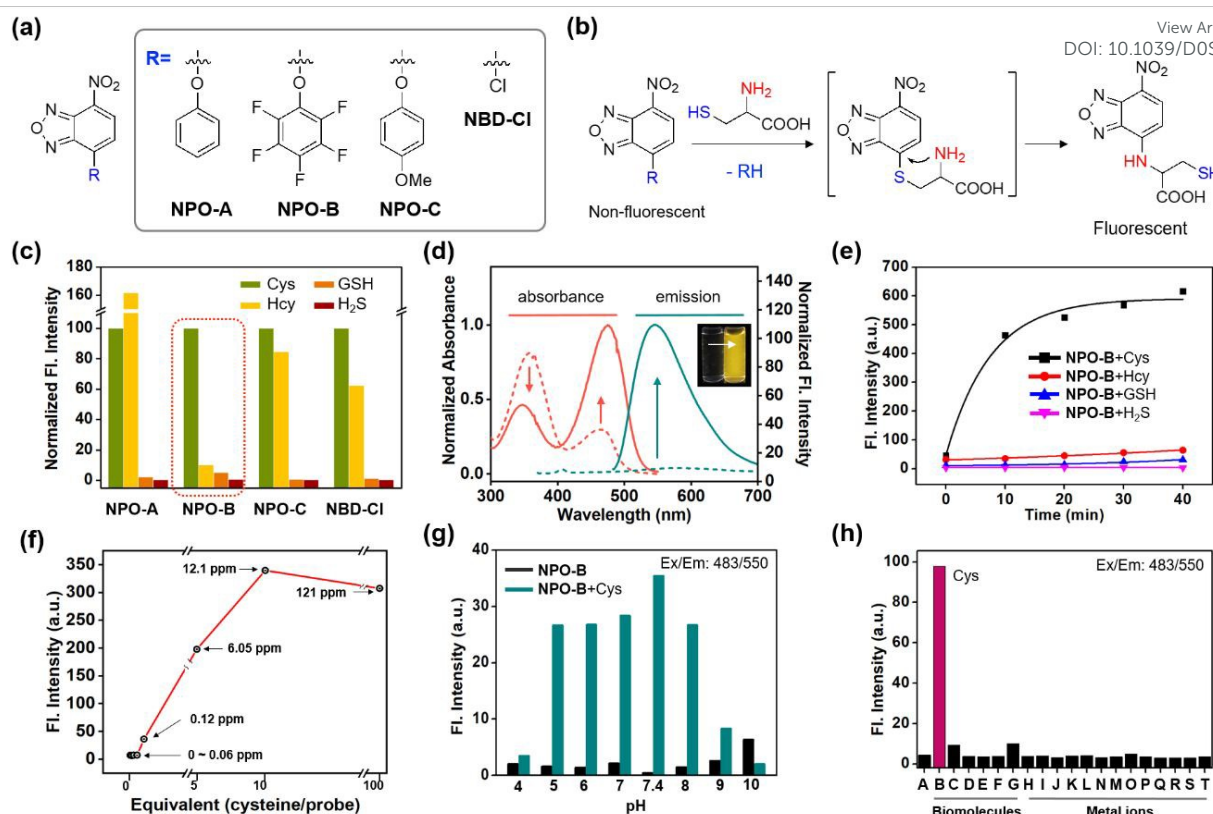


## Figures



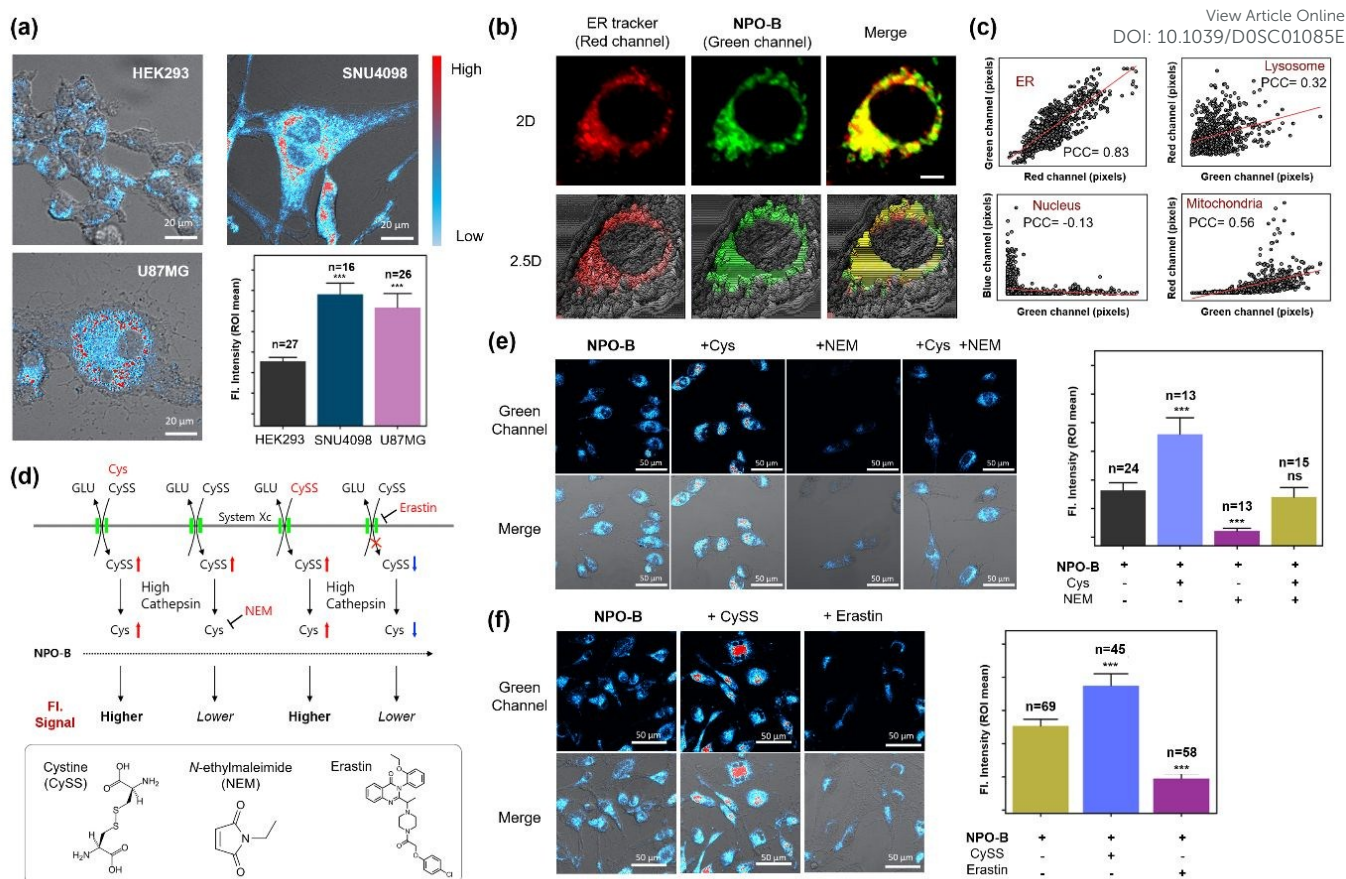
**Fig. 1.** A schematic representation of GBM and Cys-related cellular mechanism, our research rational for GBM identification. (a) 3D illustration and human MRI image for GBM site. (b) Schematic drawing of the cells in the GBM site. Reactive-oxygen species (ROS) up-regulation in hypoxia condition at the distal region from the blood vessel, as well as at the late stage of GBM. Box: ROS effect in the GBM and normal cells. (c) Up-regulated ROS mediated mechanism in the intracellular region. The up-regulation and down-regulation are indicated in red and blue arrows. Green box: endoplasmic reticulum (ER). (d) Rational in this work. NPO-B probe consisted of a signaling unit (fluorescence) and pentafluorophenol unit (Cys responsive, ER targetable). The Smiles rearrangement with Cys induced the fluorescence as a turn-on manner. The inset describes the clinical surgery of GBM patient and treatment of NPO-B probe for pathological analysis.





**Fig. 2.** Structure, working mechanism, and photophysical property analysis of NPO probe. (a) Chemical structure of NPO probes and control compound (NBD-Cl). (b) Working mechanism (Smiles rearrangement) of the NPO probes. (c) Normalized fluorescence intensity (peak height at 550 nm) of NPO probes (10  $\mu$ M) with biothiols (Cys, Hcy, GSH, and H<sub>2</sub>S, 50  $\mu$ M). The emission values were obtained under the excitation at 478 nm. (d) Normalized absorbance and emission spectra changes of NPO-B (10  $\mu$ M) with Cys (50  $\mu$ M). The absorption and emission spectra of NPO-B with Cys were measured on DI H<sub>2</sub>O containing 1% DMSO. (e) Time-dependent fluorescent intensity plot (peak height at 550 nm) of NPO-B (10  $\mu$ M) with biothiols (50  $\mu$ M). (f) Fluorescent intensity plot (peak height at 550 nm) of NPO-B (10  $\mu$ M) with low concentration of Cys. (g) Fluorescent intensity plot (peak height at 550 nm) of NPO-B (10  $\mu$ M) with Cys (50  $\mu$ M) in various pHs (pH 4–10). (h) Fluorescent intensity plot (peak height at 550 nm) of NPO-B (10  $\mu$ M) with biomolecules and metal ions (50  $\mu$ M). (A) NPO-B only, (B) L-Cys, (C) DL-Hcy, (D) L-GSH, (E) L-Glu, (F) L-Lys, (G) human serum albumin, (H) PbCl<sub>2</sub>, (I) MgCl<sub>2</sub>, (J) FeCl<sub>3</sub>, (K) Hg(NO<sub>3</sub>)<sub>2</sub>, (L) CdCl<sub>2</sub>, (M) ZnCl<sub>2</sub>, (N) NiCl<sub>2</sub>, (O) CoCl<sub>2</sub>, (P) NaCl, (Q) AuCl<sub>3</sub>, (R) AgCl, (S) CuCl<sub>2</sub>, and (T) KCl. The emission spectra were recorded under excitation at the maximum absorption wavelength. All the spectrum and intensity data was recorded in DI H<sub>2</sub>O for 30 min incubation with substrate at 37  $^{\circ}$ C.

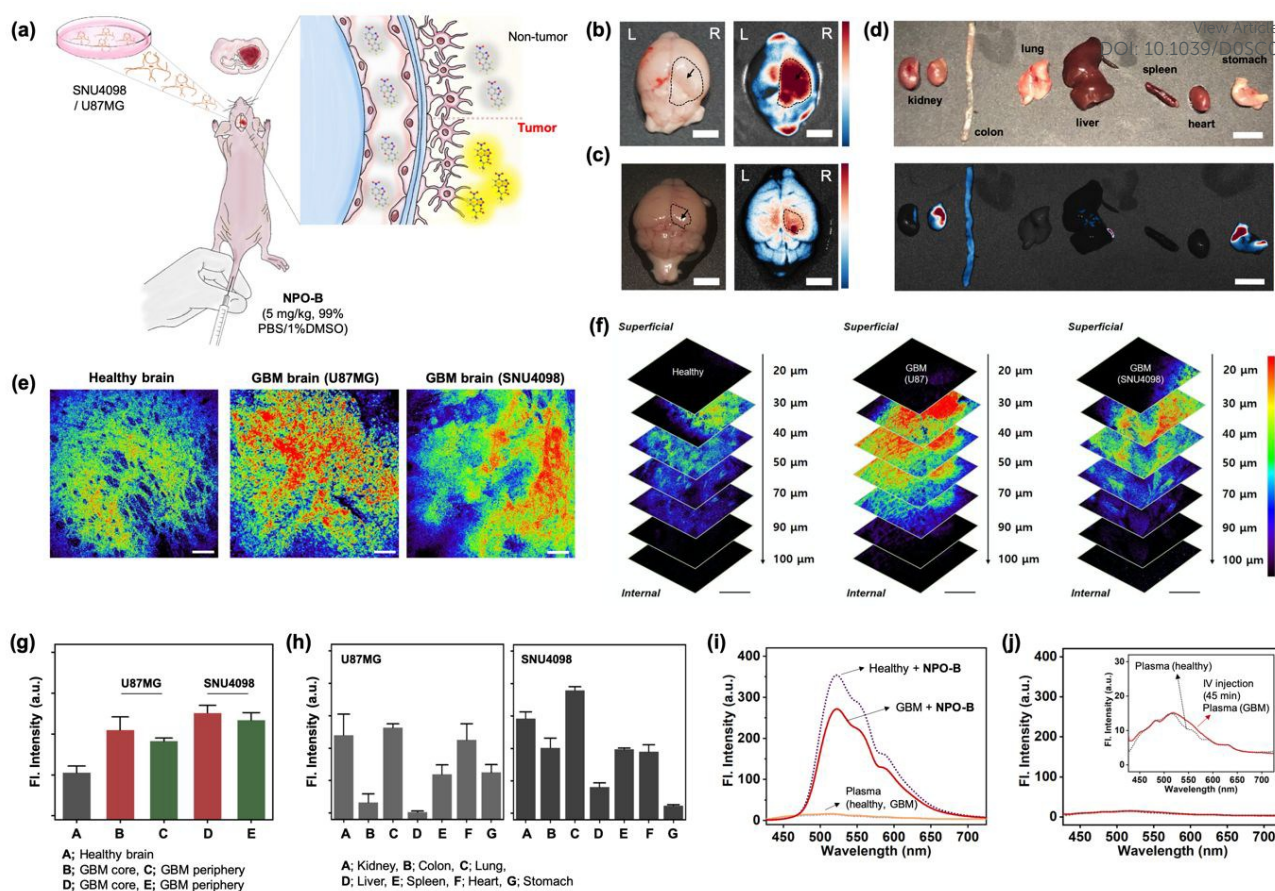




**Fig. 3.** Image-based GBM cell line identification study. (a) CLSM images of cell lines treated with NPO-B; HEK293, SNU4098 and U87MG. Cells were incubated with NPO-B (30  $\mu\text{M}$ ) for 30 min. Scale bar: 20  $\mu\text{m}$ . The fluorescence intensities represent ROI mean values (ROI was obtained by drawing whole cell based on DIC image). (b) CLSM images of U87MG treated ER-Tracker (red) and NPO-B (green). The yellow color represent overlapped regions of green and red signals. Scale bar: 5  $\mu\text{m}$ . (c) Linear fitting plot to obtain pearson correlation coefficient (PCC) in various organelles. Each pixel intensities were collected in whole cells by using ZEN 2.3 lite program, respectively (See Fig. S17 for CLSM images related PCC of each organelle). (d) Cys-related biological mechanism with CySS, NEM, and Erastin. Inset box: chemical structure of CySS, NEM, and erastin. (e) Left: CLSM images of SNU4098 cells treated NPO-B (30  $\mu\text{M}$ ) with Cys (500  $\mu\text{M}$ ), NEM (500  $\mu\text{M}$ ), and Cys with NEM. Right: Relative fluorescence intensities of each cells (each error bar represents mean  $\pm$  SD, n=number of cells, ns=non-significant, \*\*\*P < 0.001). (f) Left: CLSM images of SNU4098 cells treated NPO-B (30  $\mu\text{M}$ ) with CySS (600  $\mu\text{M}$ ) and erastin (20  $\mu\text{M}$ ), respectively. Right: Relative fluorescence intensities of each cells (each error bar represents mean  $\pm$  SD, n=number of cells, \*\*\*P < 0.001). All experiments were performed in triplicate and repeated three times independently. An intensity-based pseudo-color was applied in panel (a), (e) and (f) for better visualization. The intensity in cell was measured on Image-J program by drawing ROI over whole cell based on DIC image.

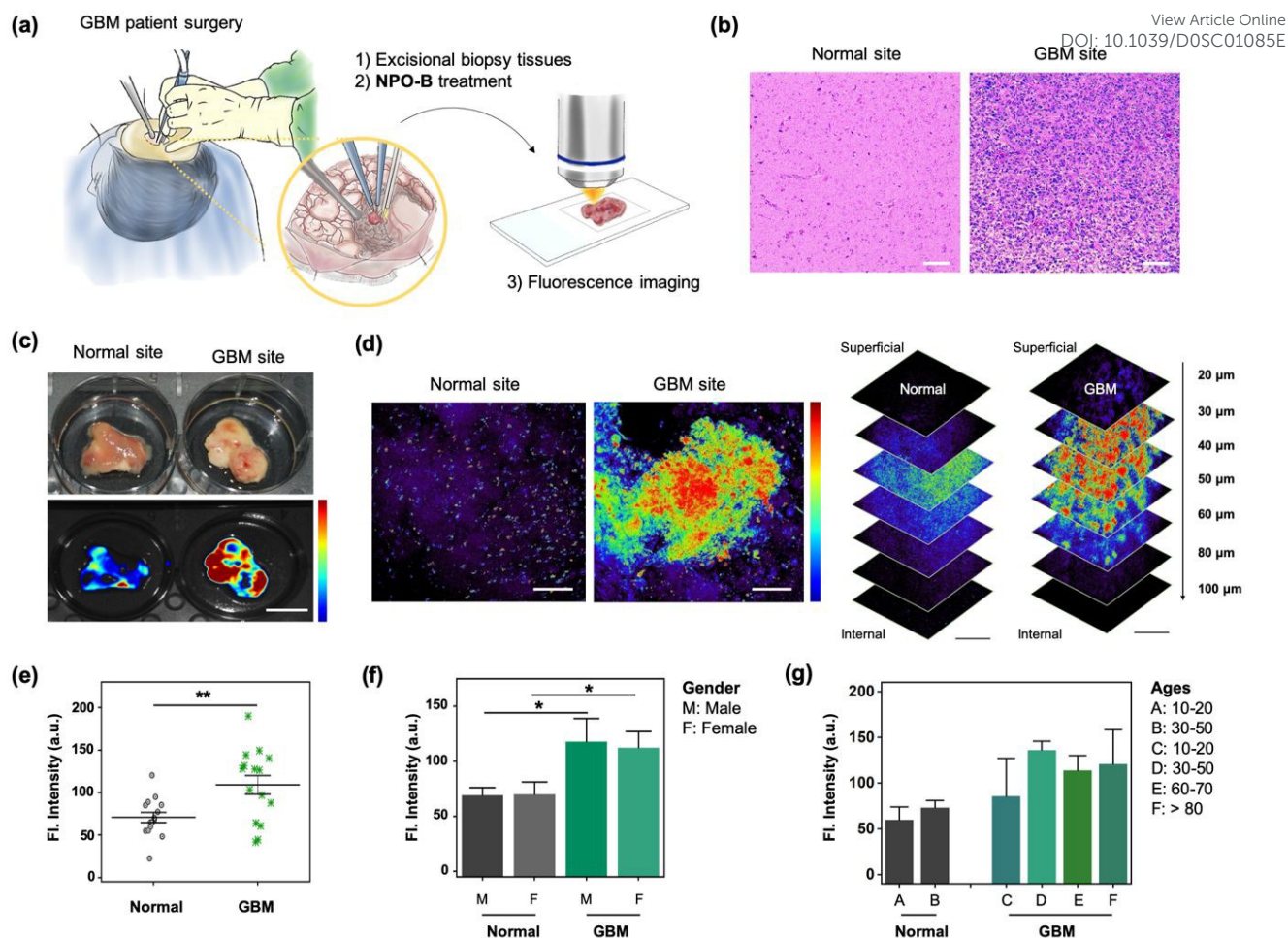






**Fig. 4.** GBM identification in xenograft animal model. (a) Schematic illustration for the application of NPO-B towards the GBM animal model; GBM cells-implanted (SNU4098, U87MG). (b) Ex vivo bright field image (left) and FTIS image (right) of the brain for U87MG-implanted mouse, after NPO-B injection (i.v.) and 45 min circulation. (c) Ex vivo naked image (left) and FTIS image (right) of the brain for SNU4098-implanted mouse after NPO-B injection (i.v.) and 45 min circulation. See Supplementary Fig. S22 for the ex vivo FTIS images of control group (healthy mouse). (d) Ex vivo bright field image (upper) and FTIS image (bottom) of dissected organs of U87MG-implanted mouse after NPO-B injection (i.v.) and 45 min circulation. (e) TPM images of the mouse brain after the treatment of NPO-B (100  $\mu$ M); healthy, U87MG-implanted and SNU4098-implanted. The images were acquired at a middle depth ( $\sim 50$   $\mu$ m) of the tissues. (f) TPM images of brain tissue in panel (e) at the indicated depths (0–100  $\mu$ m). (g) Relative fluorescence intensities of healthy brain tissues and GBM (core, periphery). All fluorescence intensities were analyzed by Image-J; each error bar represents mean  $\pm$  SEM. (h) TPM intensity plot of the GBM mouse organs (See Fig. S23–S24 for TPM images). (i) Emission spectra from the isolated mouse plasma (1/3 diluted in PBS buffer) and its NPO-B mixture (10  $\mu$ M, 30 min incubation at 37  $^{\circ}$ C). (j) Emission spectra from the isolated mouse plasma (1/3 diluted in PBS buffer) pre-treated with NPO-B (i.v., 45 min circulation).

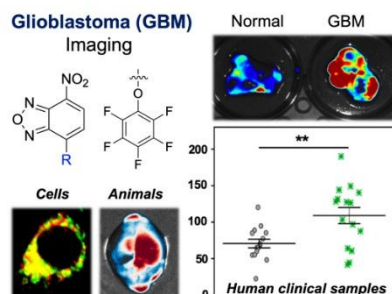




**Fig. 5.** Practical application for the GBM clinical samples. (a) Experimental scheme for the excisional biopsy tissues, isolated from the GBM patient's surgery and treatment of NPO-B. (b) Haematoxylin and eosin (H&E) stained human brain tissue sections from the normal and GBM tissue. Scale bar = 100  $\mu\text{m}$ . (c) Bright field (upper) and the FTIS images (bottom) of freshly isolated brain tissue from the normal and GBM tissue treated with NPO-B [100  $\mu\text{M}$ , 30 min, 37°C, PBS buffer (pH 7.4)]. (d) TPM images of tissue samples in panel (c). See the experimental conditions in Method Section. Scale bars = 100  $\mu\text{m}$ . The stacked TPM images of tissues acquired following the indicated vertical depths (0–100  $\mu\text{m}$ ). Scale bar is 200  $\mu\text{m}$ . See Supplementary Fig. S25 for additional TPM images for normal and GBM ( $n=15$ , each). The fluorescence images were overlaid with pseudo-color (rainbow). (e) Fluorescence intensity plot from TPM images of the brain tissues obtained at normal ( $n=15$ ) and GBM ( $n=15$ ) site, each error bar represents mean  $\pm$  SEM,  $**P < 0.01$ . (f, g) Fluorescence intensity plot from TPM images by sex and age. Gender: 8 males, 7 females in the normal group, and 6 males and 9 females in the GBM group. Each error bar represents mean  $\pm$  SEM. vs. normal male, vs. normal female,  $*P < 0.05$ . Ages of the group are categorized into six groups (A–F). Each error bar represents mean  $\pm$  SEM based on TP intensities.



## Table of Contents

**Penta-fluorophenol: A Smiles rearrangement-inspired cysteine-selective fluorescent probe for imaging of human glioblastoma**

A fluorescent molecular probe for the identification of glioblastoma is developed. The probe allows the tracing of cysteine (Cys) level in the human-derived cells, mouse xenograft model, as well as within on-site human clinical biopsy samples, which recognize Cys as a new biomarker of GBM.